

$^{14}\text{N}/^{15}\text{N}$ abundance ratio toward massive star-forming regions with different Galactic distances

Chang Ruan¹, Junzhi Wang¹, Chao Ou¹, Juan Li^{2,3}, Bo Zhang^{2,3}

¹ Guangxi Key Laboratory for Relativistic Astrophysics, School of Physical Science and Technology, Guangxi University, Nanning 530004, China

e-mail: junzhiwang@gxu.edu.cn, changruan@st.gxu.edu.cn

² Shanghai Astronomical Observatory, Chinese Academy of Sciences, 80 Nandan Road, Shanghai, 200030, China

³ Key Laboratory of Radio Astronomy, Chinese Academy of Sciences, Nanjing 210033, China

Received xx; accepted xxx

ABSTRACT

Context. The abundance ratio of $^{14}\text{N}/^{15}\text{N}$ is, in principle, a powerful tool for tracing stellar nucleosynthesis.

Aims. This work aims to measure and analyze $(^{14}\text{N}/^{15}\text{N}) \times (^{13}\text{C}/^{12}\text{C})$ and $^{14}\text{N}/^{15}\text{N}$ abundance ratios in massive star-forming regions across a range of galactocentric distances to provide constraints on galactic chemical evolution (GCE) models.

Methods. We present H^{13}CN and HC^{15}N $J=2-1$ results toward 51 massive star-forming regions obtained with the Institut de Radioastronomie Millimétrique (IRAM) 30 meter telescope. We used these results to derive $(^{14}\text{N}/^{15}\text{N}) \times (^{13}\text{C}/^{12}\text{C})$ abundance ratios as well as $^{14}\text{N}/^{15}\text{N}$ ratios using the double isotope method.

Results. We find an overall decreasing trend in the $(^{14}\text{N}/^{15}\text{N}) \times (^{13}\text{C}/^{12}\text{C})$ abundance ratio and an increasing trend in the $^{14}\text{N}/^{15}\text{N}$ ratio with increasing galactocentric distance (D_{GC}), which provides a good constraint for the GCE model based on high signal to noise ratio measurements. While the predicted $(^{14}\text{N}/^{15}\text{N}) \times (^{13}\text{C}/^{12}\text{C})$ ratios between 6 and 12 kpc determined using current GCE models are consistent with our observational results, the ratios from models for D_{GC} less than 6 kpc are significantly higher than the observational results, which indicates GCE models for $^{14}\text{N}/^{15}\text{N}$ and/or $^{13}\text{C}/^{12}\text{C}$ ratios need to be updated for at least this range.

Key words. stars: evolution – ISM: abundances – Galaxy: abundances – Galaxy: evolution.

1. Introduction

Galactic chemical evolution (GCE) models, which track the distribution of chemical elements of the interstellar medium in galaxies and their formation in stars (Matteucci 2021), help us understand the evolution of stars and galaxies (Tinsley 1980; Matteucci 2021). Carbon, nitrogen, and oxygen in the interstellar medium originate from the evolution of stars via nucleosynthesis processes (Burbidge et al. 1957; Wallerstein et al. 1997). The triple- α capture process leads to the formation of ^{12}C (Salpeter 1952), while isotopes ^{13}C , ^{15}N , and ^{17}O are produced in hydrogen-burning zones through either the cold or hot CNO cycles (Wiescher et al. 2010; Romano 2022 provides a comprehensive review of CNO nucleosynthesis in stars). Throughout their evolutionary phases, stars release these nucleosynthetic products into the surrounding medium, notably during the asymptotic giant branch and supernova phases (see, e.g., Nomoto et al. 2013; Di Criscienzo et al. 2016; Woosley 2019).

The isotopic abundance ratios of carbon, nitrogen, and oxygen depend heavily on the growth history of the Galactic disk and thus exhibit strong evolutionary features (e.g., Romano & Matteucci 2003; Romano et al. 2017). On various timescales, stars with variable initial masses and chemical compositions create isotopes of different species in varying amounts (Tinsley 1979; Wannier 1980). Hence, measuring the isotopic abundance ratio is an efficient method for tracing the chemical history and constraining GCE models (Wilson & Rood 1994; Romano 2022). For example, the $^{12}\text{C}/^{13}\text{C}$ ratio is the consequence of contributions from stars of varying masses, which collectively con-

tribute to the current radial gradient in the Milky Way over different timescales (Milam et al. 2005; Yan et al. 2019). The $^{18}\text{O}/^{17}\text{O}$ ratio can be used to trace stellar nucleosynthesis and metal enrichment processes (Henkel et al. 1994; Wilson & Rood 1994; Jiménez-Donaire et al. 2017; Ou et al. 2023). The $^{14}\text{N}/^{15}\text{N}$ ratio can also be used to study stellar nucleosynthesis and constrain the latest GCE models (Ritchey et al. 2015; Colzi et al. 2022). ^{14}N is produced through processes like hot bottom burning in asymptotic giant branch stars (Renzini & Voli 1981; Romano 2022) and the cold CNO cycle during hydrogen-burning stages (Colzi et al. 2018b), while ^{15}N is mainly formed in nova outbursts via the hot CNO cycle (Clayton 2003; Colzi et al. 2018b).

The abundance ratio of isotopes can be obtained using three alternative approaches: the singly substituted molecules, doubly substituted molecules, and double isotope methods (Wampfler et al. 2014). For the singly substituted molecules method, which involves molecules such as $\text{CN}/\text{C}^{15}\text{N}$ (see, e.g., Adande & Ziurys 2012; Ritchey et al. 2015; Sun et al. 2024), the main isotopologs are usually abundant, resulting in strong lines. However, a high abundance frequently means a high optical depth, which must be corrected via radiative transfer modeling or the intensity ratios of the hyperfine transitions (Wampfler et al. 2014). The lines of doubly substituted molecules such as $\text{C}^{18}\text{O}/^{13}\text{C}^{18}\text{O}$ (see, e.g., Paron et al. 2018; Jiménez-Donaire et al. 2017) are usually very weak as a result of their low abundances. The double isotope method, which involves, for example, $\text{HN}^{13}\text{C}/\text{H}^{15}\text{NC}$ or $\text{H}^{13}\text{CN}/\text{HC}^{15}\text{N}$ (see, e.g., Adande & Ziurys 2012; Wampfler et al. 2014; Colzi et al. 2018a,b, 2022), avoids the high opacities of the main isotopolog and the weak lines of doubly substi-

tuted molecules. However, the abundance ratio of $^{12}\text{C}/^{13}\text{C}$ must be known to derive the $^{14}\text{N}/^{15}\text{N}$ ratio.

We used the double isotope method to derive $^{14}\text{N}/^{15}\text{N}$ ratios from the intensity ratio of $\text{H}^{13}\text{CN}/\text{HC}^{15}\text{N}$ J=2-1 lines. Assuming H^{13}CN and HC^{15}N 2-1 to be optically thin with similar excitation properties, the abundance ratios of $^{14}\text{N}/^{15}\text{N}$ can be derived from velocity-integrated intensities of $\text{H}^{13}\text{CN}/\text{HC}^{15}\text{N}$ 2-1 by multiplying by $^{12}\text{C}/^{13}\text{C}$ (see, e.g., Goldsmith et al. 1981; Wampfler et al. 2014) as a function of D_{GC} ,

$$\frac{^{14}\text{N}}{^{15}\text{N}} = \frac{\int T_{\text{mb}} dv (\text{H}^{13}\text{CN})}{\int T_{\text{mb}} dv (\text{HC}^{15}\text{N})} \times \frac{^{12}\text{C}}{^{13}\text{C}}. \quad (1)$$

The $^{12}\text{C}/^{13}\text{C}$ value in each source was obtained from Sun et al. (2024) as

$$^{12}\text{C}/^{13}\text{C} = (4.08_{-0.43}^{+0.86}) \text{ kpc}^{-1} \times D_{\text{GC}} + (18.8_{-6.6}^{+2.6}). \quad (2)$$

We report the abundance ratios of $^{14}\text{N}/^{15}\text{N}$ derived using the double isotope method from data obtained with the Institut de Radioastronomie Millimétrique (IRAM) 30 m telescope toward 51 massive star-forming regions. The IRAM 30 m observations are described in Sect. 2. Section 3 provides a description of the main results. A discussion and our conclusions are presented in Sects. 4 and 5.

2. Observation

2.1. IRAM 30 m observations

The sample of 51 late-stage massive star-forming regions with parallactic distances from Reid et al. (2014, 2019) was selected to observe the spectral lines of H^{13}CN J=2-1 at 172.6778512 GHz and HC^{15}N J=2-1 at 172.1079571 GHz using the IRAM 30 meter telescope on Pico Veleta, Spain. The observations were carried out in June 2016, October 2016, and August 2017, except for G211.59+01.05, which was observed in August 2020. These sources, except for G211.59+01.05, are the same as those presented in Li et al. (2022) for NH_2D molecules. The 2 mm (E1) band of the Eight Mixer Receiver (EMIR) and the Fourier Transform Spectrometers (FTS) backend were used to cover from about 166.0 GHz to 173.8 GHz with 195 kHz channel spacing and dual polarization. The standard position-switching mode with an azimuth OFF of -600 arcsec was used.

The IRAM 30 m telescope, with a beam size of ~ 14.3 arcsec at 172 GHz and a typical system temperature of 400 K in the 2 mm band, utilizes nearby quasi-stellar objects for pointing correction every two hours. Focus was checked and corrected at the start of each run, as well as during sunsets and sunrises. The main beam brightness temperature (T_{mb}) was calculated using $T_{\text{mb}} = T_{\text{A}}^* \cdot F_{\text{eff}}/B_{\text{eff}}$, where T_{A}^* is the antenna temperature, the forward efficiency (F_{eff}) is 0.93, and the beam efficiency (B_{eff}) is 0.73 for the 2 mm band. Each scan lasted 2 minutes, and the total on-source time ranged from 12 to 234 minutes per source.

2.2. Data reduction

Data reduction was based on the CLASS package in the GILDAS¹ software, a comprehensive tool designed for (sub)millimeter radio-astronomical applications, which facilitates the efficient manipulation and visualization of spectra. GILDAS is widely used to process data from the IRAM 30

m telescope and the Northern Extended Millimeter Array (NOEMA), excluding very long-baseline interferometry observations. The spectra from each source were averaged into one spectrum using the CLASS package and subtracted from a first-order baseline. The spectra in each source were plotted on the same velocity scale to facilitate comparisons between H^{13}CN and HC^{15}N J=2-1. The line fluxes were determined through a direct integration of the emission lines, with errors calculated using the equation $\sigma = \text{rms} \sqrt{\delta v \cdot \Delta v}$, where δv represents the channel separation in velocity, Δv the velocity range for integration, and rms the root mean square noise obtained with baseline fitting for each spectrum with δv channel spacing.

3. Results

The spectra with $T_{\text{peak}} > 3\sigma$ at 195 kHz channel spacing, which corresponds to 0.34 km s^{-1} at 172 GHz, were considered detections, where T_{peak} is peak T_{mb} and σ is the rms noise. Neither H^{13}CN J=2-1 nor HC^{15}N J=2-1 were detected in IRAS 05137+3919 or G012.90-00.24. HC^{15}N J=2-1 was not detected, while a clear double-peak structure of H^{13}CN J=2-1 was found in Sgr B2, which was likely due to the self-absorption of hot core regions (see, e.g., Adande & Ziurys 2012). Both H^{13}CN J=2-1 and HC^{15}N J=2-1 lines were contaminated by nearby lines in G010.47+00.02, which hindered the use of these two lines for scientific analysis. H^{13}CN J=2-1 and HC^{15}N J=2-1 were detected and included in the ratio calculations for the remaining 47 sources.

The velocity-integrated intensities of H^{13}CN J=2-1 range from $1.6 \pm 0.03 \text{ K km s}^{-1}$ in G211.59+01.05 to $115.7 \pm 0.7 \text{ K km s}^{-1}$ in G005.88-00.39, with a mid-value of $10.9 \pm 0.1 \text{ K km s}^{-1}$, as shown in Table A.1. The velocity-integrated intensities of HC^{15}N J=2-1 range from $0.3 \pm 0.03 \text{ K km s}^{-1}$ in G211.59+01.05 to $38.2 \pm 0.2 \text{ K km s}^{-1}$ in W51M, with a mid-value of $2.4 \pm 0.1 \text{ K km s}^{-1}$.

The hyperfine structure (hfs) of H^{13}CN 2-1 (Fuchs et al. 2004; Cazzoli & Puzzarini 2005) can cause an overestimation of line widths if single-component Gaussians are used. Thus, only full widths at half maximum (FWHMs) of HC^{15}N J=2-1 in each source were derived through single-component Gaussian fitting using the CLASS package. The derived FWHMs of HC^{15}N J=2-1 range from $2.0 \pm 0.2 \text{ km s}^{-1}$ in G183.72-03.66 to $15.8 \pm 0.2 \text{ km s}^{-1}$ in W49N, with a mid-value of $4.6 \pm 0.5 \text{ km s}^{-1}$. Obvious hfs features of H^{13}CN J=2-1 were found in 16 sources with HC^{15}N J=2-1 FWHMs less than 5.3 km s^{-1} , but they were blurred into component due to line broadening. Figure 1a shows an example of this, with the H^{13}CN J=2-1 spectrum in G081.87+00.78. Another example (G081.75+00.59), in which the hfs feature of H^{13}CN J=2-1 can be distinguished, is shown in Fig. 1b.

The line ratio of $\text{H}^{13}\text{CN}/\text{HC}^{15}\text{N}$ 2-1 can be used as the abundance ratio of $(^{14}\text{N}/^{15}\text{N}) \times (^{13}\text{C}/^{12}\text{C})$ (Goldsmith et al. 1981), assuming the molecular isotopic abundances ratio represents the isotopic ratio of elements, the same excitation condition as H^{13}CN and HC^{15}N molecules, and both lines are optically thin. The relationship between the $(^{14}\text{N}/^{15}\text{N}) \times (^{13}\text{C}/^{12}\text{C})$ abundance ratio derived from the $\text{H}^{13}\text{CN}/\text{HC}^{15}\text{N}$ 2-1 line ratio and D_{GC} , as well as the $^{14}\text{N}/^{15}\text{N}$ ratios and D_{GC} , is presented in Fig. 2. The D_{GC} values range from 3.3 kpc in G009.62+00.19 to 11.9 kpc in G211.59+01.05 (Reid et al. 2014, 2019). The $(^{14}\text{N}/^{15}\text{N}) \times (^{13}\text{C}/^{12}\text{C})$ ratio varies from 2.5 ± 0.02 in W51M to 9.2 ± 0.8 in G023.44-00.18. The unweighted linear regression fits to these data were obtained as follows:

$$(^{14}\text{N}/^{15}\text{N}) \times (^{13}\text{C}/^{12}\text{C}) = (-0.2 \pm 0.1) \text{ kpc}^{-1} \times D_{\text{GC}} + (6.0 \pm 0.9),$$

¹ <http://www.iram.fr/IRAMFR/GILDAS>

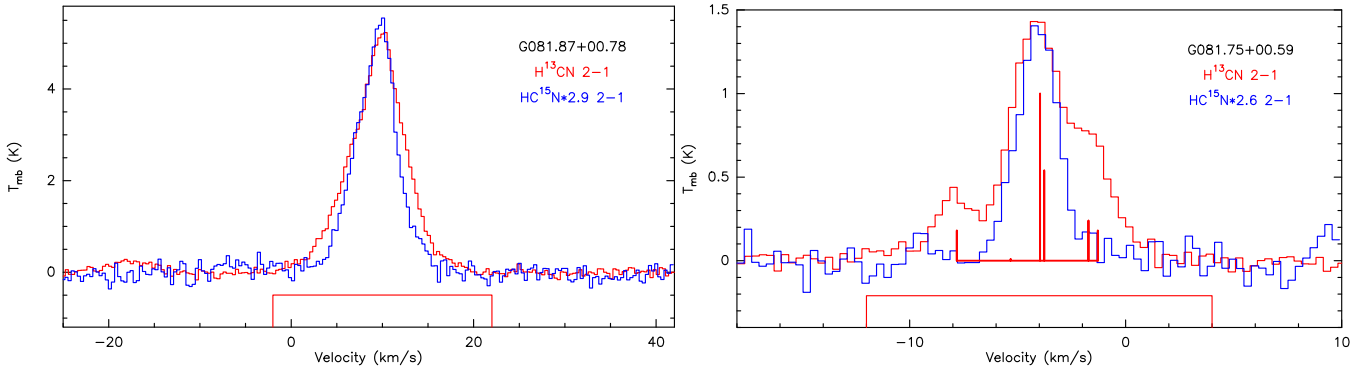


Fig. 1. Spectra of H^{13}CN $J=2-1$ and HC^{15}N $J=2-1$ for two sources as examples. Left: H^{13}CN $J=2-1$ hfs in G081.87+00.78 cannot be resolved due to line broadening. Right: H^{13}CN $J=2-1$ hfs in G081.75+00.59 can be resolved with a narrow line width. The vertical bold red lines indicate the hyperfine transitions for H^{13}CN $J=2-1$: $F=1-1, 1-2, 3-2, 2-1, 1-0,$ and $2-2$ (from left to right).

with a correlation coefficient of -0.34 .

The relation between D_{GC} and the $^{14}\text{N}/^{15}\text{N}$ ratio, derived from the $(^{14}\text{N}/^{15}\text{N}) \times (^{13}\text{C}/^{12}\text{C})$ ratio by multiplying by Eq. (2), spans from $109.6^{+19.8}_{-22.9}$ in W51M to $344.6^{+74.2}_{-80.1}$ in G034.39+00.22. It is presented in Fig. 2b. The unweighted linear regression fits for these data are

$$^{14}\text{N}/^{15}\text{N} = (10.8 \pm 6.0) \text{ kpc}^{-1} \times D_{\text{GC}} + (141.1 \pm 43.8). \quad (4)$$

As shown in Figs. 2a and 2b, there is a significant decreasing trend in $(^{14}\text{N}/^{15}\text{N}) \times (^{13}\text{C}/^{12}\text{C})$ and an increasing trend in $^{14}\text{N}/^{15}\text{N}$ ratios with increasing D_{GC} . The $(^{14}\text{N}/^{15}\text{N}) \times (^{13}\text{C}/^{12}\text{C})$ ratio versus the heliocentric distance instead of D_{GC} is presented in Fig. 3, which does not show any significant trend.

4. Discussion

The $(^{14}\text{N}/^{15}\text{N}) \times (^{13}\text{C}/^{12}\text{C})$ ratios derived from the observed $\text{H}^{13}\text{CN}/\text{HC}^{15}\text{N}$ $2-1$ line ratio versus D_{GC} in these 47 sources are compared with four GCE models, shown in Fig. 2, with D_{GC} ranging from 4 to 12 kpc with data points for each 2 kpc (Colzi et al. 2022), in which different initial mass ranges for nova system white dwarf progenitors and various masses ejected in the form of ^{13}C and ^{15}N in each outburst were considered. The decreasing trend in the $(^{14}\text{N}/^{15}\text{N}) \times (^{13}\text{C}/^{12}\text{C})$ ratio with increments of D_{GC} in the four models is consistent with our observational results (see Fig. 2a). On the other hand, the poor correlation coefficient between the $(^{14}\text{N}/^{15}\text{N}) \times (^{13}\text{C}/^{12}\text{C})$ ratio and the source distance (see Fig. 3) indicates that the decreasing trend in the $(^{14}\text{N}/^{15}\text{N}) \times (^{13}\text{C}/^{12}\text{C})$ ratio with increments of D_{GC} is not caused by observational effects of difference source distances to the Sun.

The overall model values of the $(^{14}\text{N}/^{15}\text{N}) \times (^{13}\text{C}/^{12}\text{C})$ ratio are higher than the measured ones (see Fig. 2a), which may be caused by the underestimation of the $\text{H}^{13}\text{CN}/\text{HC}^{15}\text{N}$ ratio since H^{13}CN $J=2-1$ lines are not really optically thin in many sources, especially for sources with strong H^{13}CN $2-1$ emission. There are six sources with peak H^{13}CN $2-1$ T_{mb} values higher than 4 K. Because of the possible underestimation of the $\text{H}^{13}\text{CN}/\text{HC}^{15}\text{N}$ ratio caused by the moderate opacity of H^{13}CN $J=2-1$, our observational results in the range 6-12 kpc should be considered to be generally consistent with the models since they follow a similar trend. However, the $(^{14}\text{N}/^{15}\text{N}) \times (^{13}\text{C}/^{12}\text{C})$ ratios predicted by all four models are significantly higher than the observational results, except for that in G023.44-00.18, which has a large error bar. We suggest that the model results of the $^{14}\text{N}/^{15}\text{N}$ and/or

(3) $^{13}\text{C}/^{12}\text{C}$ ratios at 4 kpc need to be updated. Similar results of low $(^{14}\text{N}/^{15}\text{N}) \times (^{13}\text{C}/^{12}\text{C})$ ratios in three sources (IRAS 15567-5236, IRAS 17160-3707, and IRAS 17220-3609) with small D_{GC} had been reported, with H^{13}CN and HC^{15}N $1-0$ observations (Dahmen et al. 1995). However, no scientific comparisons of observational and model results are available for these sources (Dahmen et al. 1995), mainly because the models had not been developed by that time.

The $^{14}\text{N}/^{15}\text{N}$ ratio in each source can be derived using the already obtained $(^{14}\text{N}/^{15}\text{N}) \times (^{13}\text{C}/^{12}\text{C})$ ratios and the $^{13}\text{C}/^{12}\text{C}$ ratio, which is unknown. We obtained the $^{14}\text{N}/^{15}\text{N}$ ratio of each source by assuming the $^{13}\text{C}/^{12}\text{C}$ ratio is related to D_{GC} and using the fitting result from Sun et al. (2024), which we plot in Fig. 2b. The slightly tighter correlation between the $^{14}\text{N}/^{15}\text{N}$ and the D_{GC} , with a correlation coefficient of 0.42, than that of $(^{14}\text{N}/^{15}\text{N}) \times (^{13}\text{C}/^{12}\text{C})$ and D_{GC} , with a correlation coefficient of -0.34 , is due to the use of the $^{13}\text{C}/^{12}\text{C}$ ratio from the fitting result in Sun et al. (2024). An accurate $^{14}\text{N}/^{15}\text{N}$ ratio for each source should be obtained with the measured $^{13}\text{C}/^{12}\text{C}$ value in individual sources. Even though the comparison between measured and model ratios of $(^{14}\text{N}/^{15}\text{N}) \times (^{13}\text{C}/^{12}\text{C})$ versus D_{GC} should be more accurate than that of the $^{14}\text{N}/^{15}\text{N}$ ratio versus D_{GC} , due to the uncertainties of the assumed $^{13}\text{C}/^{12}\text{C}$ ratio, the relation between $^{14}\text{N}/^{15}\text{N}$ and D_{GC} (see Fig. 2b) can help us find the differences between the four models. When the assumed $^{13}\text{C}/^{12}\text{C}$ ratio from Sun et al. (2024) is similar to that of the real value in each source, the $^{14}\text{N}/^{15}\text{N}$ ratios from observational results are generally consistent with models 1 and 2. However, they are significantly different to that at 4 and 6 kpc with models 3 and 4, which should therefore be updated.

The range in D_{GC} in our sample is similar to that in Colzi et al. (2018b), while sources with D_{GC} from 12 kpc to 19 kpc were included in Colzi et al. (2022). However, the $(^{14}\text{N}/^{15}\text{N}) \times (^{13}\text{C}/^{12}\text{C})$ ratio has much lower uncertainties thanks to the longer typical observing time on each source than that in Colzi et al. (2018b), and as such our results can better constrain predicted $(^{14}\text{N}/^{15}\text{N}) \times (^{13}\text{C}/^{12}\text{C})$ and $^{14}\text{N}/^{15}\text{N}$ ratios from GCE models, especially when D_{GC} is less than 6 kpc, using the values measured in each source. Future observations with other tracers, which can avoid optically thick effects, will be useful for deriving more accurate $^{14}\text{N}/^{15}\text{N}$ ratios than observations with H^{13}CN lines. GCE models of the relation between chemical abundances and D_{GC} were also tested with various tracers in ionized gas, such as radio recombination lines (RRLs; Balser et al. 2011), RRLs and optical lines (Méndez-Delgado et al. 2022), and RRLs and infrared hfs lines (Pineda et al. 2024). The rela-

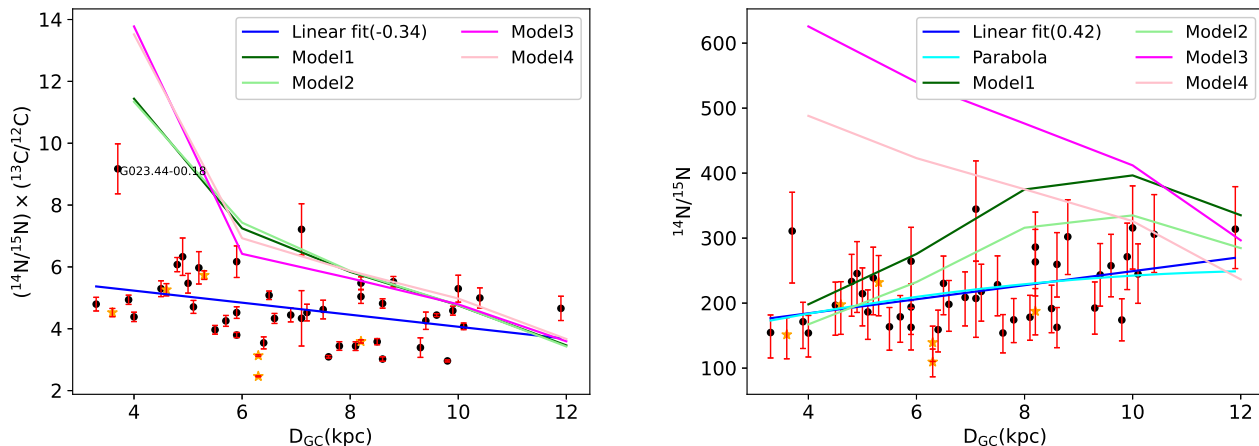


Fig. 2. Abundance ratios of $(^{14}\text{N}/^{15}\text{N}) \times (^{13}\text{C}/^{12}\text{C})$ (left) and $^{14}\text{N}/^{15}\text{N}$ with D_{GC} (right). The filled black circles are sources with peak T_{mb} of H^{13}CN 2-1 lower than 4K, and the orange stars sources with peak T_{mb} higher than 4 K. The blue lines are linear fitting results. The cyan parabola was obtained by multiplying the linear regression fit of $(^{14}\text{N}/^{15}\text{N}) \times (^{13}\text{C}/^{12}\text{C})$ given in Eq. (3) by the $^{12}\text{C}/^{13}\text{C}$ ratio (Eq. 2). The green, dark green, pink, and magenta lines are the models from Colzi et al. (2022).

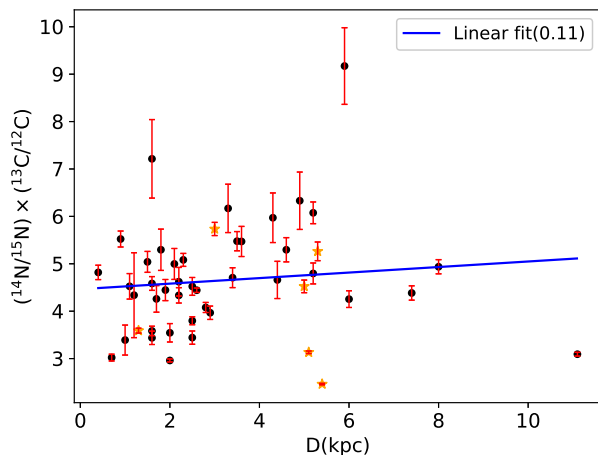


Fig. 3. Abundance ratio of $(^{14}\text{N}/^{15}\text{N}) \times (^{13}\text{C}/^{12}\text{C})$ versus heliocentric distance. The symbols are the same as in Fig. 2, and the blue line is the linear fitting result.

tionship between N/H and D_{GC} shows a clear gradient in regions of D_{GC} greater than 6 kpc, consistent with GCE models, while large scatter is found for D_{GC} less than ~ 6 kpc (Pineda et al. 2024). The He, C, N, O, Ne, S, Cl, and Ar abundances varying with D_{GC} (Méndez-Delgado et al. 2022) agrees well with GCE models for D_{GC} greater than 6 kpc; however, they lack data points with D_{GC} less than 6 kpc, mainly because of dust obscuration in the Galactic plane. Thus, isotopic ratios in the regions with D_{GC} less than 6 kpc in molecular gas derived with millimeter wavelengths are ideal for constraining GCE models.

5. Summary and conclusion

H^{13}CN 2-1 and HC^{15}N 2-1 lines are detected in 47 of the 51 massive star-forming regions observed with the IRAM 30m telescope, and they were used to derive the abundance ratios of $(^{14}\text{N}/^{15}\text{N}) \times (^{13}\text{C}/^{12}\text{C})$ as well as $^{14}\text{N}/^{15}\text{N}$ via the double isotope method and assumed $^{13}\text{C}/^{12}\text{C}$ ratio. The $(^{14}\text{N}/^{15}\text{N}) \times (^{13}\text{C}/^{12}\text{C})$ ra-

tio shows a decreasing trend with increasing D_{GC} , while no trend is found for this ratio and distance from the Sun. The $^{14}\text{N}/^{15}\text{N}$ ratio shows an increasing trend with increasing D_{GC} . With a small error bar for the measured $(^{14}\text{N}/^{15}\text{N}) \times (^{13}\text{C}/^{12}\text{C})$ ratio, our results can constrain the GCE model of $(^{14}\text{N}/^{15}\text{N}) \times (^{13}\text{C}/^{12}\text{C})$ well, especially for D_{GC} less than 6kpc; for that range, updated GCE models are needed.

Acknowledgements. We thank Dr. Donatella Romano for helpful discussion and provide the data GCE model. This work is supported by National Key R&D Program of China under grant 2023YFA1608204 and the National Natural Science Foundation of China grant 12173067. This work is based on observations carried out under project numbers 012-16, 023-17, and 005-20, with the IRAM 30m telescope. IRAM is supported by INSU/CNRS (France), MPG (Germany) and IGN (Spain).

References

- Adande, G. R. & Ziurys, L. M. 2012, *ApJ*, 744, 194
 Balser, D. S., Rood, R. T., Bania, T. M., & Anderson, L. D. 2011, *ApJ*, 738, 27
 Burbidge, E. M., Burbidge, G. R., Fowler, W. A., & Hoyle, F. 1957, *Reviews of Modern Physics*, 29, 547
 Cazzoli, G. & Puzzarini, C. 2005, *Journal of Molecular Spectroscopy*, 233, 280
 Clayton, D. 2003, *Handbook of Isotopes in the Cosmos* (Cambridge, UK: Cambridge University Press)
 Colzi, L., Fontani, F., Caselli, P., et al. 2018a, *A&A*, 609, A129
 Colzi, L., Fontani, F., Rivilla, V. M., et al. 2018b, *MNRAS*, 478, 3693
 Colzi, L., Romano, D., Fontani, F., et al. 2022, *A&A*, 667, A151
 Dahmen, G., Wilson, T. L., & Matteucci, F. 1995, *A&A*, 295, 194
 Di Criscienzo, M., Ventura, P., García-Hernández, D. A., et al. 2016, *MNRAS*, 462, 395
 Fuchs, U., Brünken, S., Fuchs, G., et al. 2004, *Zeitschrift für Naturforschung A*, 59, 861
 Goldsmith, P. F., Langer, W. D., Ellender, J., Kollberg, E., & Irvine, W. 1981, *ApJ*, 249, 524
 Henkel, C., Wilson, T. L., Langer, N., Chin, Y. N., & Mauersberger, R. 1994, in *The Structure and Content of Molecular Clouds*, ed. T. L. Wilson & K. J. Johnston, Vol. 439, 72–88
 Jiménez-Donaire, M. J., Cormier, D., Bigiel, F., et al. 2017, *ApJ*, 836, L29
 Li, Y., Wang, J., Li, J., Liu, S., & Luo, Q. 2022, *MNRAS*, 512, 4934
 Matteucci, F. 2021, *A&A Rev.*, 29, 5
 Méndez-Delgado, J. E., Amayo, A., Arellano-Córdova, K. Z., et al. 2022, *MNRAS*, 510, 4436
 Milam, S. N., Savage, C., Brewster, M. A., Ziurys, L. M., & Wyckoff, S. 2005, *ApJ*, 634, 1126
 Nomoto, K., Kobayashi, C., & Tominaga, N. 2013, *ARA&A*, 51, 457
 Ou, C., Wang, J., Zheng, S., et al. 2023, *MNRAS*, 522, 559

- Paron, S., Areal, M. B., & Ortega, M. E. 2018, *A&A*, 617, A14
- Pineda, J. L., Horiuchi, S., Anderson, L. D., et al. 2024, *ApJ*, 973, 89
- Reid, M. J., Menten, K. M., Brunthaler, A., et al. 2019, *ApJ*, 885, 131
- Reid, M. J., Menten, K. M., Brunthaler, A., et al. 2014, *ApJ*, 783, 130
- Renzini, A. & Voli, M. 1981, *A&A*, 94, 175
- Ritchey, A. M., Federman, S. R., & Lambert, D. L. 2015, *ApJ*, 804, L3
- Romano, D. 2022, *A&A Rev.*, 30, 7
- Romano, D. & Matteucci, F. 2003, *MNRAS*, 342, 185
- Romano, D., Matteucci, F., Zhang, Z.-Y., Papadopoulos, P. P., & Ivison, R. J. 2017, *MNRAS*, 470, 401
- Salpeter, E. E. 1952, *ApJ*, 115, 326
- Sun, Y., Zhang, Z.-Y., Wang, J., et al. 2024, *MNRAS*
- Tinsley, B. M. 1979, *ApJ*, 229, 1046
- Tinsley, B. M. 1980, *Fund. Cosmic Phys.*, 5, 287
- Wallerstein, G., Iben, I., Parker, P., et al. 1997, *Reviews of Modern Physics*, 69, 995
- Wampfler, S. F., Jørgensen, J. K., Bizzarro, M., & Bisschop, S. E. 2014, *A&A*, 572, A24
- Wannier, P. G. 1980, *ARA&A*, 18, 399
- Wiescher, M., Görres, J., Uberseder, E., Imbriani, G., & Pignatari, M. 2010, *Annual Review of Nuclear and Particle Science*, 60, 381
- Wilson, T. L. & Rood, R. 1994, *ARA&A*, 32, 191
- Woosley, S. E. 2019, *ApJ*, 878, 49
- Yan, Y. T., Zhang, J. S., Henkel, C., et al. 2019, *ApJ*, 877, 154

Appendix A: Data parameters

Table A.1. Source names, equatorial coordinates, distances, molecular species, and ratio data.

Source Alias	R.A. (hh:mm:ss)	Decl. (dd:mm:ss)	D (kpc)	D_{GC} (kpc)	Line (2-1)	$\int T_{mb} dv$ (K·km s ⁻¹)	Velocity range (km s ⁻¹)	Rms (10 ⁻² K)	T_{peak} (K)	V_{LSR} (km s ⁻¹)	$(^{14}N/^{15}N) \times (^{13}C/^{12}C)$	$^{14}N/^{15}N$
G005.88-00.39	18:00:30.31	-24:04:04.5	3.0	5.3	H ¹³ CN	115.73(0.69)	-10 40	16.8	10.2	10.02(0.03)	5.73(0.14)	231.8(^{+41.43} _{-51.22})
					HC ¹⁵ N	20.18(0.47)	3 18	21.0	3.4	9.29(0.06)		
G009.62+00.19	18:06:14.66	-20:31:31.7	5.2	3.3	H ¹³ CN	32.77(0.39)	-11 18	12.4	2.51	4.62(0.07)	4.8(0.22)	154.74(^{+27.04} _{-39.11})
					HC ¹⁵ N	6.83(0.3)	-7 15	11.1	0.96	3.77(0.12)		
G010.62-00.38	18:10:28.55	-19:55:48.6	5.0	3.6	H ¹³ CN	63.45(0.44)	-20 20	11.9	6.21	-4.54(0.03)	4.52(0.13)	151.48(^{+26.15} _{-37.13})
W 31					HC ¹⁵ N	14.03(0.4)	-20 20	10.9	1.86	-3.49(0.06)		
G011.49-01.48	18:16:22.13	-19:41:27.2	1.2	7.1	H ¹³ CN	7.02(0.37)	5 17	18.5	1.41	10.39(0.11)	4.34(0.9)	207.2(^{+57.06} _{-59.86})
					HC ¹⁵ N	1.62(0.32)	5 15	17.5	0.57	10.16(0.21)		
G011.91-00.61	18:13:58.12	-18:54:20.3	3.4	5.1	H ¹³ CN	12.49(0.15)	20 50	4.65	0.95	35.91(0.07)	4.71(0.21)	186.42(^{+33.91} _{-42.21})
					HC ¹⁵ N	2.65(0.11)	27 48	4.26	0.3	35.48(0.17)		
G012.80-00.20	18:14:14.23	-17:55:40.5	2.9	5.5	H ¹³ CN	13.68(0.13)	20 50	4.07	1.21	36.19(0.04)	3.97(0.14)	163.59(^{+29.65} _{-36.03})
					HC ¹⁵ N	3.45(0.12)	25 50	4.04	0.61	35.35(0.06)		
G012.88+00.48	18:11:51.42	-17:31:29.0	2.5	5.9	H ¹³ CN	17.12(0.12)	23 49	3.89	1.84	33.21(0.04)	3.8(0.08)	162.83(^{+29.37} _{-34.89})
IRAS 18089-1732					HC ¹⁵ N	4.51(0.09)	25 41	4.04	0.79	33.23(0.08)		
G012.90-00.26	18:14:39.57	-17:52:00.4	2.5	5.9	H ¹³ CN	18.87(0.22)	23 52	7.17	2.04	38.19(0.04)	4.52(0.19)	193.92(^{+35.63} _{-42.11})
					HC ¹⁵ N	4.17(0.17)	30 45	7.35	0.77	37.83(0.08)		
G014.33-00.64	18:18:54.67	-16:47:50.3	1.1	7.2	H ¹³ CN	27.57(0.62)	6 35	19.8	3.09	22.41(0.07)	4.52(0.27)	217.96(^{+41.84} _{-45.74})
					HC ¹⁵ N	6.09(0.34)	15 27	16.6	1.43	22.13(0.09)		
G015.03-00.67	18:20:24.81	-16:11:35.3	2.0	6.4	H ¹³ CN	9.02(0.17)	10 27	7.25	1.7	19.52(0.04)	3.54(0.19)	159.17(^{+30.01} _{-34.27})
M 17					HC ¹⁵ N	2.54(0.13)	13 25	6.45	0.78	19.23(0.06)		
G016.58-00.05	18:21:09.08	-14:31:48.8	3.6	5.0	H ¹³ CN	11.54(0.17)	47 73	5.56	1.28	59.77(0.05)	5.47(0.32)	214.45(^{+39.75} _{-49.46})
					HC ¹⁵ N	2.11(0.12)	52 68	5.09	0.38	59.94(0.12)		
G023.00-00.41	18:34:40.20	-09:00:37.0	4.6	4.5	H ¹³ CN	11.04(0.14)	65 90	4.64	1.03	78.22(0.06)	5.3(0.26)	196.78(^{+35.55} _{-46.18})
					HC ¹⁵ N	2.08(0.1)	70 85	4.3	0.28	77.62(0.17)		
G023.44-00.18	18:34:39.19	-08:31:25.4	5.9	3.7	H ¹³ CN	8.39(0.13)	88 115	4.14	0.74	103.01(0.08)	9.17(0.81)	310.88(^{+59.69} _{-79.96})
					HC ¹⁵ N	0.91(0.08)	97 107	4.31	0.22	102.16(0.15)		
G027.36-00.16	18:41:51.06	-05:01:43.4	8.0	3.9	H ¹³ CN	18.71(0.15)	79 110	4.59	1.6	92.45(0.06)	4.94(0.15)	171.39(^{+29.85} _{-41.2})
					HC ¹⁵ N	3.79(0.11)	80 110	3.46	0.39	92.85(0.12)		
G028.86+00.06	18:43:46.22	-03:35:29.6	7.4	4.0	H ¹³ CN	10.63(0.11)	87 113	3.71	1.09	103.92(0.04)	4.38(0.15)	153.97(^{+27.01} _{-36.86})
					HC ¹⁵ N	2.43(0.08)	95 112	3.31	0.33	103.64(0.1)		
G029.95-00.01	18:46:03.74	-02:39:22.3	5.3	4.6	H ¹³ CN	37.16(0.4)	85 110	13.9	4.08	97.88(0.04)	5.26(0.2)	197.7(^{+35.29} _{-43.74})
W 43S					HC ¹⁵ N	7.06(0.25)	90 105	11.2	1.07	97.79(0.1)		
G031.28+00.06	18:48:12.39	-01:26:30.7	4.3	5.2	H ¹³ CN	10.92(0.24)	100 116	10.5	1.22	109.1(0.1)	5.97(0.52)	238.94(^{+47.13} _{-56.76})
					HC ¹⁵ N	1.83(0.15)	105 113	9.39	0.39	109.16(0.21)		
G031.58+00.07	18:48:41.68	-01:09:59.0	4.9	4.9	H ¹³ CN	6.99(0.14)	88 103	6.04	0.89	96.39(0.08)	6.33(0.61)	245.55(^{+49.11} _{-59.91})
W 43Main					HC ¹⁵ N	1.1(0.1)	90 103	4.91	0.29	96.48(0.14)		
G032.04+00.05	18:49:36.58	-00:45:46.9	5.2	4.8	H ¹³ CN	15.38(0.15)	85 112	5.05	1.36	95.51(0.05)	6.08(0.23)	233.18(^{+41.81} _{-53.36})
					HC ¹⁵ N	2.53(0.09)	90 102	4.56	0.4	96.01(0.12)		
G034.39+00.22	18:53:18.77	01:24:08.8	1.6	7.1	H ¹³ CN	3.6(0.09)	48 67	3.48	0.51	57.42(0.07)	7.21(0.83)	344.6(^{+74.22} _{-80.09})
					HC ¹⁵ N	0.5(0.06)	52 62	3.04	0.13	57.13(0.18)		
G035.02+00.34	18:54:00.67	02:01:19.2	2.3	6.5	H ¹³ CN	12.11(0.09)	40 62	3.32	1.46	52.69(0.03)	5.08(0.14)	230.33(^{+42.08} _{-48.15})
					HC ¹⁵ N	2.38(0.06)	45 59	2.82	0.39	52.46(0.07)		
G035.19-00.74	18:58:13.05	01:40:35.7	2.2	6.6	H ¹³ CN	17.55(0.2)	22 44	7.48	1.82	33.99(0.05)	4.33(0.16)	198.18(^{+36.62} _{-41.57})
					HC ¹⁵ N	4.05(0.14)	23 42	5.65	0.64	33.23(0.09)		
G035.20-01.73	19:01:45.54	01:13:32.5	3.3	5.9	H ¹³ CN	5.92(0.08)	36 50	3.81	1.08	43.58(0.03)	6.17(0.51)	264.46(^{+52.15} _{-60.46})
					HC ¹⁵ N	0.96(0.08)	37 50	3.72	0.29	43.27(0.09)		
G037.43+01.51	18:54:14.35	04:41:41.7	1.9	6.9	H ¹³ CN	7.67(0.11)	35 52	4.78	1.3	44.15(0.03)	4.45(0.22)	208.73(^{+39.36} _{-43.8})
					HC ¹⁵ N	1.73(0.08)	38 50	4.09	0.49	43.97(0.06)		
G043.16+00.01	19:10:13.41	09:06:12.8	11.1	7.6	H ¹³ CN	44.25(0.24)	-20 35	5.59	2.54	5.19(0.04)	3.09(0.04)	154.04(^{+28.33} _{-30.58})
W 49N					HC ¹⁵ N	14.31(0.17)	-13 28	4.54	0.86	6.31(0.09)		
G043.79-00.12	19:11:53.99	09:35:50.3	6.0	5.7	H ¹³ CN	10.89(0.13)	33 56	4.6	1.14	44.41(0.05)	4.25(0.18)	178.93(^{+32.77} _{-39.21})
OH 43.8-0.1					HC ¹⁵ N	2.56(0.1)	35 52	4.22	0.39	43.44(0.11)		

Notes. The table lists the source names, aliases, and equatorial coordinates (Cols. 1-3), the heliocentric distance determined via the parallax method from Reid et al. (2014, 2019, Col. 4), the galactocentric distance (D_{GC}) calculated from the heliocentric distances (Col. 5), the molecular species data, including their velocity-integrated intensities and velocity ranges (Cols. 6-8), the rms noise level obtained through baseline fitting (Col. 9), the peak T_{mb} and central velocity derived from single Gaussian fitting of the spectra (Cols. 10-11), and the $(^{14}N/^{15}N) \times (^{13}C/^{12}C)$ and $^{14}N/^{15}N$ ratios (Cols. 12-13).

Table A.1. Continued.

Source Alias	R.A. (hh:mm:ss)	Decl. (dd:mm:ss)	D (kpc)	D_{GC} (kpc)	Line (2-1)	$\int T_{\text{mb}} dv$ (K km s $^{-1}$)	Velocity range (km s $^{-1}$)	Rms (10 $^{-2}$ K)	T_{peak} (k)	V_{LSR} (km s $^{-1}$)	$(^{14}\text{N}/^{15}\text{N}) \times (^{13}\text{C}/^{12}\text{C})$	$^{14}\text{N}/^{15}\text{N}$
G049.48-00.36 W 51 IRS2	19:23:39.82	14:31:05.0	5.1	6.3	H 13 CN	59.91(0.23)	40 80	6.35	5.5	60.47(0.03)	3.13(0.03)	139.42($^{+25.15}_{-29.19}$)
					HC 15 N	19.12(0.15)	50 75	5.04	2.18	60.38(0.07)		
G049.48-00.38 W 51M	19:23:43.87	14:30:29.5	5.4	6.3	H 13 CN	94.12(0.32)	40 80	8.8	6.84	55.63(0.09)	2.46(0.02)	109.58($^{+19.75}_{-22.93}$)
					HC 15 N	38.23(0.2)	35 77	5.26	3.2	56.48(0.2)		
G059.78+00.06	19:43:11.25	23:44:03.3	2.2	7.5	H 13 CN	5.48(0.1)	15 30	4.29	0.98	22.38(0.04)	4.62(0.3)	228.3($^{+44.4}_{-47.79}$)
					HC 15 N	1.19(0.07)	16 28	3.69	0.36	22.16(0.07)		
G069.54-00.97 ON 1	20:10:09.07	31:31:36.0	2.5	7.8	H 13 CN	8.9(0.11)	0 23	3.87	1.23	12.05(0.03)	3.44(0.14)	174.27($^{+32.81}_{-34.99}$)
					HC 15 N	2.58(0.1)	0 23	3.58	0.46	11.92(0.07)		
G075.76+00.33	20:21:41.09	37:25:29.3	3.5	8.2	H 13 CN	9.61(0.07)	-11 7	2.88	1.53	-1.7(0.02)	5.48(0.2)	286.19($^{+53.91}_{-56.46}$)
					HC 15 N	1.75(0.06)	-9 5	2.92	0.43	-1.81(0.05)		
G078.12+03.63 IRAS 20126+4104	20:14:26.07	41:13:32.7	1.6	8.1	H 13 CN	10.73(0.15)	-13 7	5.69	1.49	-3.47(0.04)	3.44(0.14)	178.26($^{+33.69}_{-34.43}$)
					HC 15 N	3.12(0.12)	-13 5	4.87	0.45	-3.71(0.11)		
G081.75+00.59 DR 21	20:39:01.99	42:24:59.3	1.5	8.2	H 13 CN	6.67(0.08)	-12 4	3.55	1.23	-3.77(0.03)	5.04(0.22)	263.4($^{+50.0}_{-52.32}$)
					HC 15 N	1.32(0.06)	-8 0	3.37	0.54	-4.06(0.04)		
G081.87+00.78 W 75N	20:38:36.43	42:37:34.8	1.3	8.2	H 13 CN	36.71(0.22)	-2 22	7.81	4.78	9.61(0.02)	3.59(0.05)	187.62($^{+34.76}_{-36.46}$)
					HC 15 N	10.22(0.13)	0 18	5.39	1.76	9.4(0.03)		
G092.67+03.07	21:09:21.73	52:22:37.1	1.6	8.5	H 13 CN	8.59(0.08)	-15 2	3.5	1.31	-6.25(0.03)	3.58(0.1)	191.64($^{+35.91}_{-37.13}$)
					HC 15 N	2.4(0.06)	-11 0	3.22	0.61	-6.23(0.04)		
G109.87+02.11 Cep A	22:56:18.10	62:01:49.5	0.7	8.6	H 13 CN	15.44(0.15)	-21 3	5.21	1.85	-10.06(0.03)	3.02(0.07)	162.8($^{+30.45}_{-31.35}$)
					HC 15 N	5.11(0.11)	-20 -1	4.36	0.81	-10.09(0.06)		
G111.54+00.77 NGC 7538	23:13:45.36	61:28:10.6	2.6	9.6	H 13 CN	15.84(0.05)	-70 -48	1.72	2.49	-57.5(0.02)	4.44(0.05)	257.51($^{+48.3}_{-47.73}$)
					HC 15 N	3.57(0.04)	-65 -51	1.63	0.77	-57.8(0.04)		
G121.29+00.65 L 1287	00:36:47.35	63:29:02.2	0.9	8.8	H 13 CN	5.76(0.04)	-27 -10	1.52	1.0	-17.33(0.01)	5.52(0.17)	302.1($^{+56.9}_{-58.08}$)
					HC 15 N	1.04(0.03)	-25 -12	1.48	0.31	-17.6(0.03)		
G123.06-06.30 NGC 281	00:52:24.70	56:33:50.5	2.8	10.1	H 13 CN	7.21(0.05)	-40 -20	2.04	1.16	-30.51(0.02)	4.08(0.11)	244.74($^{+46.47}_{-45.08}$)
					HC 15 N	1.77(0.04)	-40 -20	1.7	0.39	-30.57(0.04)		
G133.94+01.06 W 30H	02:27:03.82	61:52:25.2	2.0	9.8	H 13 CN	24.06(0.11)	-60 -37	4.01	2.78	-47.0(0.03)	2.96(0.03)	174.03($^{+32.7}_{-32.07}$)
					HC 15 N	8.13(0.08)	-55 -40	3.52	1.31	-47.02(0.03)		
G176.51+00.20	05:37:52.14	32:00:03.9	1.0	9.3	H 13 CN	1.88(0.06)	-23 -12	3.08	0.4	-18.01(0.07)	3.39(0.32)	192.41($^{+40.17}_{-40.17}$)
					HC 15 N	0.55(0.05)	-23 -14	2.78	0.17	-18.25(0.11)		
G183.72-03.66	05:40:24.23	23:50:54.7	1.8	10.0	H 13 CN	2.34(0.04)	-5 8	1.81	0.5	2.41(0.03)	5.3(0.44)	315.63($^{+64.74}_{-63.29}$)
					HC 15 N	0.44(0.04)	-3 7	1.93	0.19	1.99(0.06)		
G188.94+00.88 S 252	06:08:53.35	21:38:28.7	2.1	10.4	H 13 CN	3.99(0.07)	-3 10	3.36	0.83	3.58(0.03)	5.0(0.33)	305.95($^{+61.04}_{-58.82}$)
					HC 15 N	0.8(0.05)	-1 8	2.87	0.24	3.34(0.09)		
G192.60-00.04 S 255	06:12:54.02	17:59:23.3	1.6	9.9	H 13 CN	8.8(0.09)	0 15	3.78	1.63	7.59(0.02)	4.58(0.14)	271.37($^{+51.67}_{-50.51}$)
					HC 15 N	1.92(0.06)	1 13	2.86	0.47	7.4(0.05)		
G209.00-19.38 Orion Nebula	05:35:15.80	-05:23:14.1	0.4	8.6	H 13 CN	5.89(0.05)	2 15	2.38	1.36	8.97(0.02)	4.82(0.15)	259.64($^{+48.85}_{-50.29}$)
					HC 15 N	1.22(0.04)	3 14	1.92	0.47	8.81(0.03)		
G232.62+00.99	07:32:09.78	-16:58:12.8	1.7	9.4	H 13 CN	3.5(0.1)	10 24	4.66	0.72	17.09(0.06)	4.26(0.28)	243.43($^{+48.24}_{-48.07}$)
					HC 15 N	0.82(0.05)	14 21	3.15	0.34	17.0(0.06)		
G211.59+01.05	06:52:45.30	01:40:23.1	4.4	11.9	H 13 CN	1.55(0.03)	39 51	1.62	0.31	45.62(0.05)	4.66(0.39)	313.81($^{+65.38}_{-60.66}$)
					HC 15 N	0.33(0.03)	41 50	1.55	0.09	45.76(0.12)		

Table A.2. Same as Table A.1 but for the four sources excluded from the ratio calculations.

Source Alias	R.A. (hh:mm:ss)	Decl. (dd:mm:ss)	D (kpc)	D_{GC} (kpc)	Line (2-1)	$\int T_{\text{mb}} dv$ (K km s $^{-1}$)	Velocity range (km s $^{-1}$)	Rms (10 $^{-2}$ K)	T_{peak} (k)	V_{LSR} (km s $^{-1}$)	$(^{14}\text{N}/^{15}\text{N}) \times (^{13}\text{C}/^{12}\text{C})$	$^{14}\text{N}/^{15}\text{N}$
G000.67-00.03 Sgr B2	17:47:20.00	-28:22:40.0	7.8	0.2	H 13 CN
					HC 15 N	4.46(0.61)	45 75	19.1	0.38	57.11(0.64)		
G010.47+00.02	18:08:38.23	-19:51:50.3	8.5	1.6	H 13 CN
					HC 15 N		
G012.90-00.24	18:14:34.42	-17:51:51.9	2.5	5.9	H 13 CN	1.74(0.43)	30 45	19.1	0.23	37.37(1.0)
					HC 15 N		
G168.06+00.82 IRAS 05137+3919	05:17:13.74	39:22:19.9	7.7	15.9	H 13 CN	0.78(0.17)	-28 -22	12.2	0.26	-25.76(0.32)	1.14(0.4)	95.24($^{+38.39}_{-36.94}$)
					HC 15 N	0.68(0.19)	-32 -22	10.1	0.19	-24.76(0.34)		

Notes. IRAS 05137+3919, G012.90-00.24, Sgr B2, and G010.47+00.02 were excluded from the ratio calculations due to non-detections or contamination in the H 13 CN J=2-1 and/or HC 15 N J=2-1 lines.

Appendix B: Spectral lines

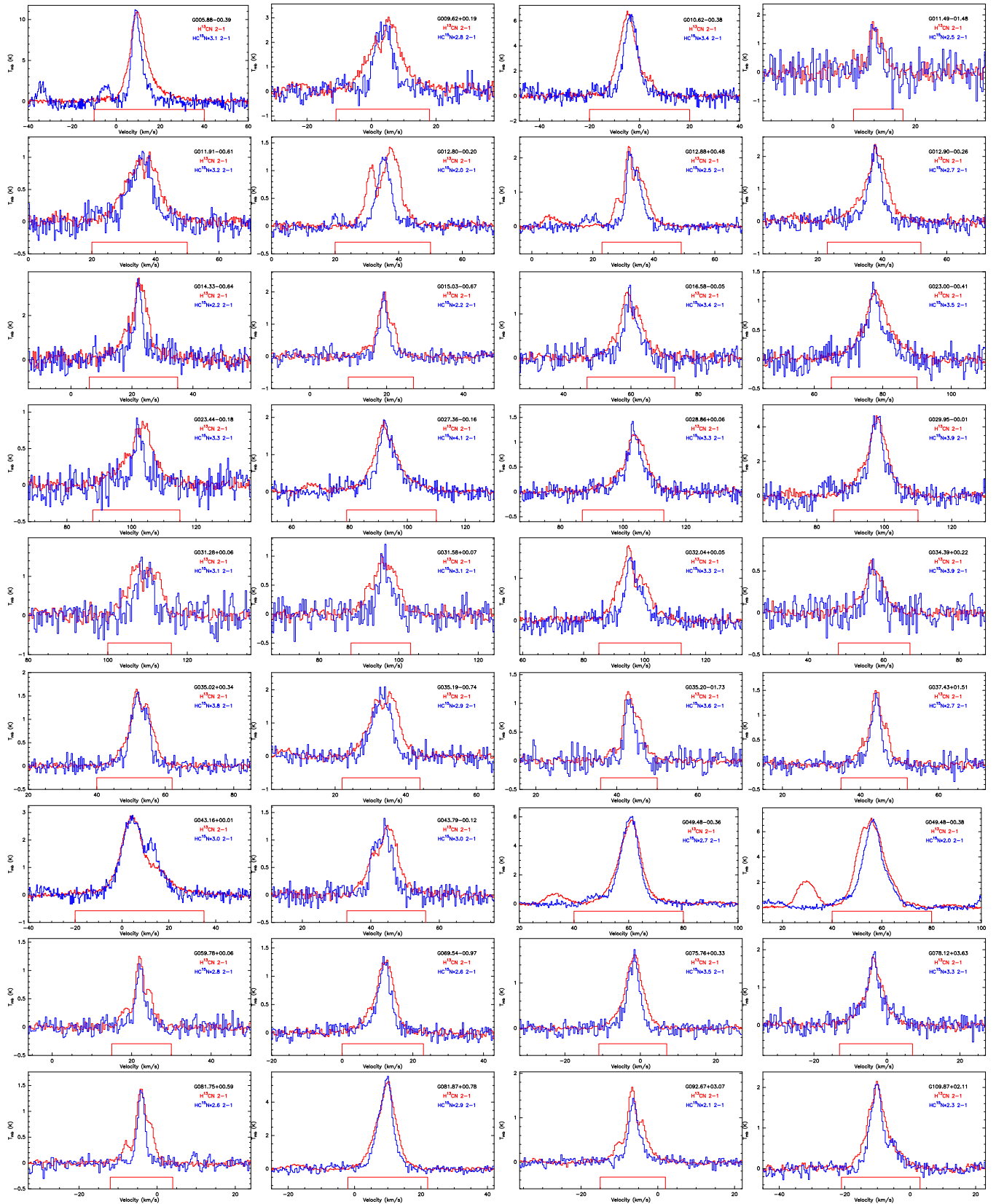


Fig. B.1. Observational results of spectra for $\text{H}^{13}\text{CN } 2-1$ and $\text{HC}^{15}\text{N } 2-1$. They are plotted on the same velocity scale for each spectrum, with the red boxes below each spectrum indicating the velocity integration range for $\text{H}^{13}\text{CN } J=2-1$.

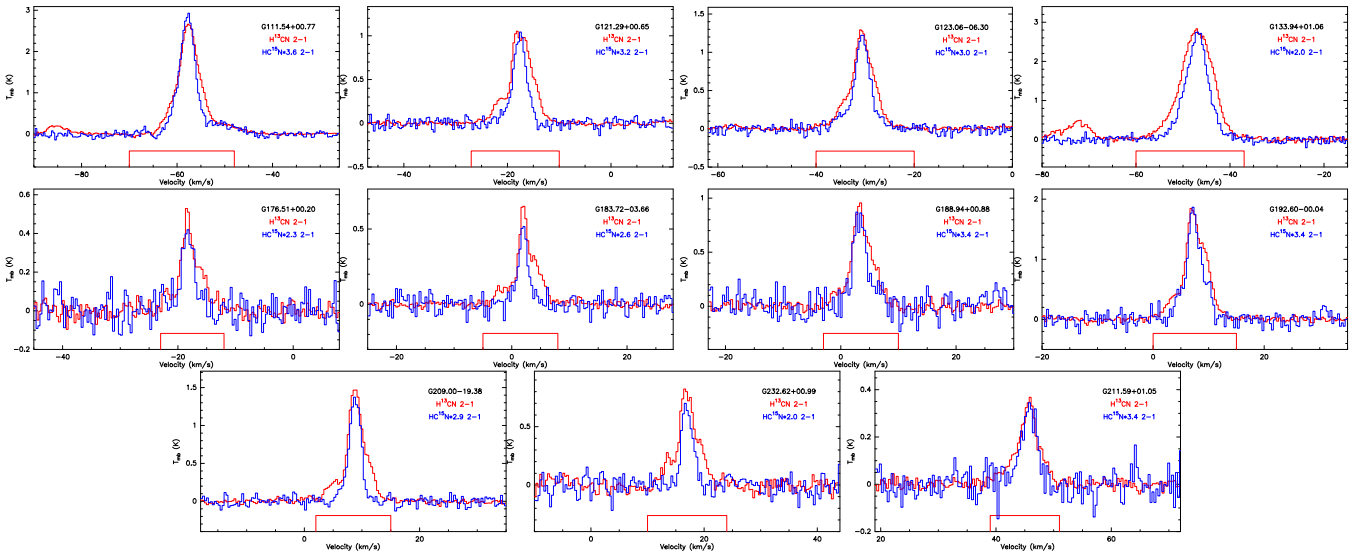


Fig. B.1. Continued.

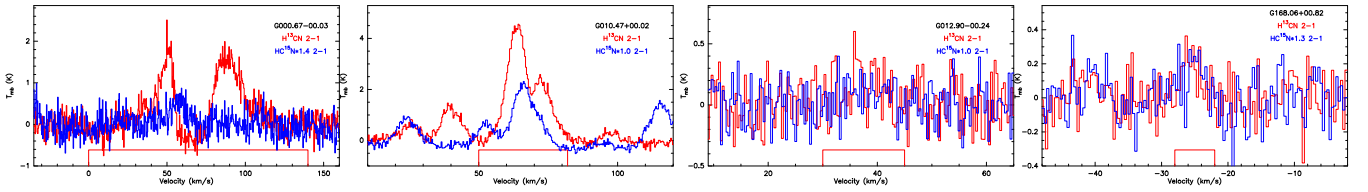


Fig. B.2. Four sources (IRAS 05137+3919, G012.90-00.24, Sgr B2, and G010.47+00.02) excluded from the ratio calculations due to non-detections or contamination in the H^{13}CN J=2-1 and/or HC^{15}N J=2-1 lines.